THE ASTRONOMICAL JOURNAL, 117:2185–2198, 1999 May

OPTICAL AND RADIO POLARIMETRY OF THE M87 JET AT 0.″2 RESOLUTION

ERIC S. PERLMAN, JOHN A. BIRETTA, FANG ZHOU, WILLIAM B. SPARKS, AND F. DUCCIO MACCHETTO
Space Telescope Science Institute, 3700 San Martin Drive, Baltimore, MD 21218
Received 1998 November 17; accepted 1999 January 13

ABSTRACT

We discuss optical (*HST*/WFPC2 F555W) and radio (15 GHz VLA) polarimetry observations of the M87 jet taken during 1994–1995. The angular resolution of both observations is ∼0.″2, which at the distance of M87 corresponds to 15 pc. Many knot regions are very highly polarized (∼40%–50%, approaching the theoretical maximum for optically thin synchrotron radiation), suggesting highly ordered magnetic fields. High degrees of polarization are also observed in interknot regions. The optical and radio polarization maps share many similarities, and in both, the magnetic field is largely parallel to the jet, except in the "shocklike" knot regions (parts of HST-1, A, and C), where it becomes perpendicular to the jet.

We do observe significant differences between the radio and optical polarized structures, particularly for bright knots in the inner jet, giving us important insight into the radial structure of the jet. Unlike in the radio, the optical magnetic field position angle becomes perpendicular to the jet at the upstream ends of knots HST-1, D, E, and F. Moreover, the optical polarization appears to decrease markedly at the position of the flux maxima in these knots. In contrast, the magnetic field position angle observed in the radio remains parallel to the jet in most of these regions, and the decreases in radio polarization are smaller. More minor differences are seen in other jet regions. Many of the differences between optical and radio polarimetry results can be explained in terms of a model whereby shocks occur in the jet interior, where higher energy electrons are concentrated and dominate both polarized and unpolarized emissions in the optical, while the radio maps show strong contributions from lower energy electrons in regions with $\boldsymbol{B}$ parallel, near the jet surface.

Key words: galaxies: active — galaxies: individual (M87) — galaxies: jets

1. INTRODUCTION

The synchrotron jet hosted by the giant elliptical galaxy M87 is perhaps the most intensely studied feature of any active galactic nucleus (AGN). Because of its brightness and proximity (distance 16 Mpc; Tonry 1991), it represents an ideal testing ground for jet models. Its large-scale radio structure (Biretta 1993; Böhringer et al. 1995) is typical of low-power FR I radio galaxies (Fanaroff & Riley 1974): the radio lobes are edge-dimmed, and a prominent, apparently one-sided jet emerges from the nucleus. No counterjet has been seen in any optical or radio image of the jet; however, there is strong evidence for its presence in the form of optical synchrotron emission at the location of a radio hot spot in the southeast (SE) lobe (Sparks et al. 1992; Stiavelli et al. 1992).

Although the gross morphology of the M87 jet is remarkably constant from the radio through the optical (Boksenberg et al. 1992), small but significant differences have been found at the highest resolutions by pre- and post-COSTAR *Hubble Space Telescope* (*HST*) observations (Sparks, Biretta, & Macchetto 1996, hereafter SBM96). In particular, the optical jet is considerably more compact than the radio jet, and the knots are more centrally concentrated. These trends appear to continue from the optical into the UV. Recent X-ray images suggest that more differences may be present in the *ROSAT* band (Neumann et al. 1997). The jet is highly polarized (Baade 1956; Warren-Smith, King, & Scarrott 1984; Schlötelburg, Meisenheimer, & Röser 1988; Fraix-Burnet, Le Borgne, & Nieto 1989), with some regions approaching the maximum possible for optically thin synchrotron radiation (∼72%) in both radio (Owen, Hardee, & Cornwell 1989, hereafter OHC89) and optical/UV (this paper; Capetti et al. 1997; Thomson et al. 1995) images. Such high polarization suggests the presence of highly ordered magnetic fields in the jet. Recent VLA observations suggest that the kiloparsec-scale lobes are also highly polarized (Zhou 1998).

High-resolution radio observations with the VLA (Biretta, Zhou, & Owen 1995, hereafter B95) have detected superluminal motions within the jet of M87 at distances of ∼200 pc from the nucleus, and speeds of ∼c up to 1200 pc from the nucleus. At smaller scales, postrefurbishment *HST* Faint Object Camera (FOC) observations in the near-UV have detected a number of new superluminal components (Biretta et al. 1998, 1999; hereafter B98, B99), with speeds ranging from 2c to 6c. It is therefore interesting that VLBI observations have yet to discover any evidence of superluminal motions on parsec scales (Biretta & Junor 1995; Reid et al. 1989). This may be due either to insufficient temporal sampling or to differences between the radio and optical structure of the jet. A VLBI monitoring campaign with rapid sampling is now underway to study this issue.

Here we present the results of *HST*/WFPC-2 optical, and VLA radio, polarimetry of the M87 jet. Both data sets were obtained during 1994–1995 and have resolution ∼0.″2, translating to 15 pc linear resolution at a distance of 16 Mpc. The optical data we present are much higher signal-to-noise ratio (S/N) than pre-COSTAR FOC and WFPC-1 polarimetry data (Thomson et al. 1995; Capetti et al. 1997), and therefore are particularly useful in revealing many new details regarding the magnetic field structure of the inner jet that were only hinted at in earlier data. They also do not suffer from the spherically aberrated point-spread function (PSF) of pre-COSTAR observations. They are, however,

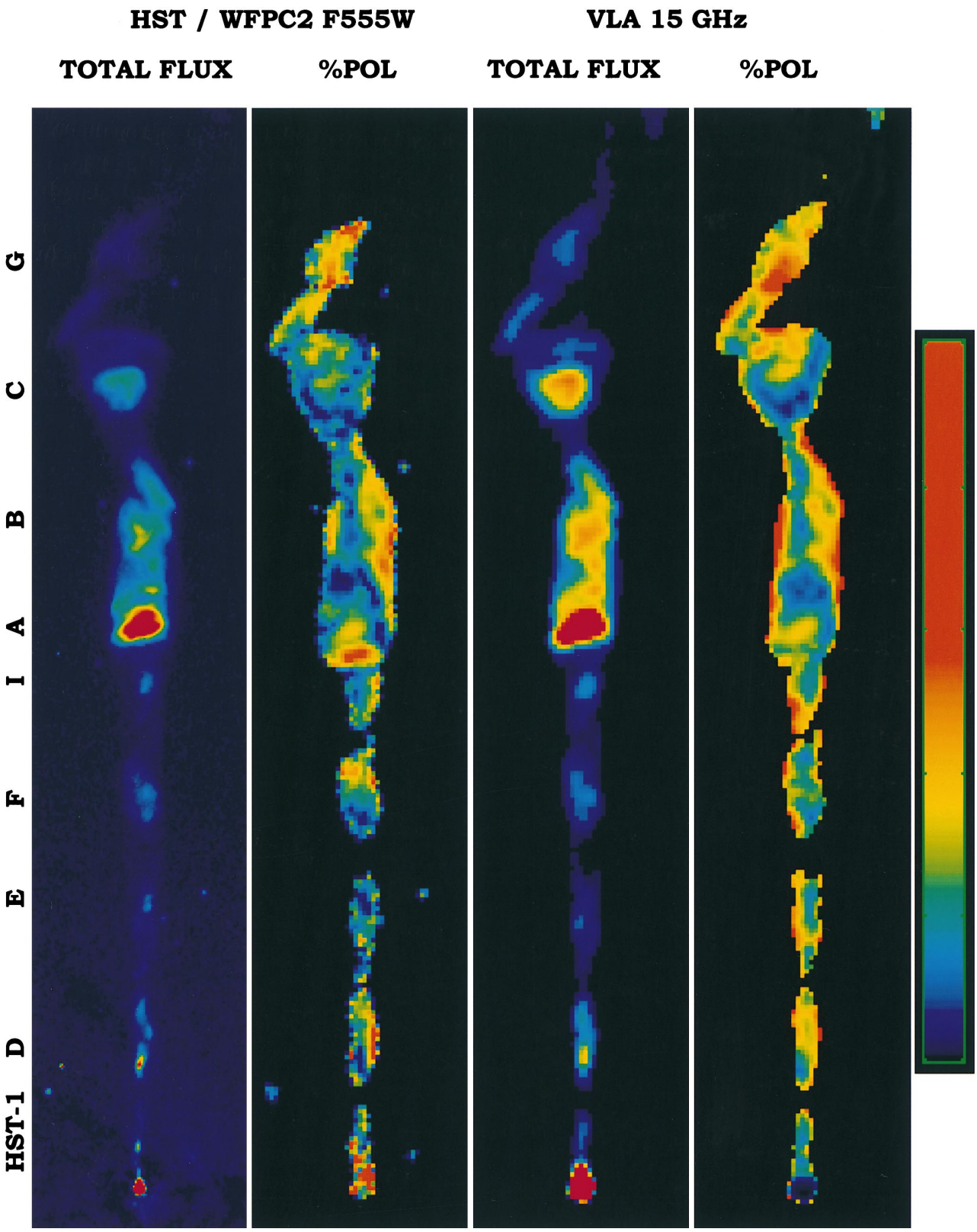

FIG. 1.—False-color representations of the total intensity and polarization of the M87 jet in the optical (*HST* F555W; *top two panels*) and radio (VLA 14.5 GHz; *bottom two panels*). The *HST* observations were carried out in 1995 May, whereas the VLA observations were done in 1994 February. All maps were rotated so that the jet is along the *x*-axis and are convolved to 0".23 resolution. At the bottom, we give the false-color scale for the two polarization panels (used for both optical and radio).

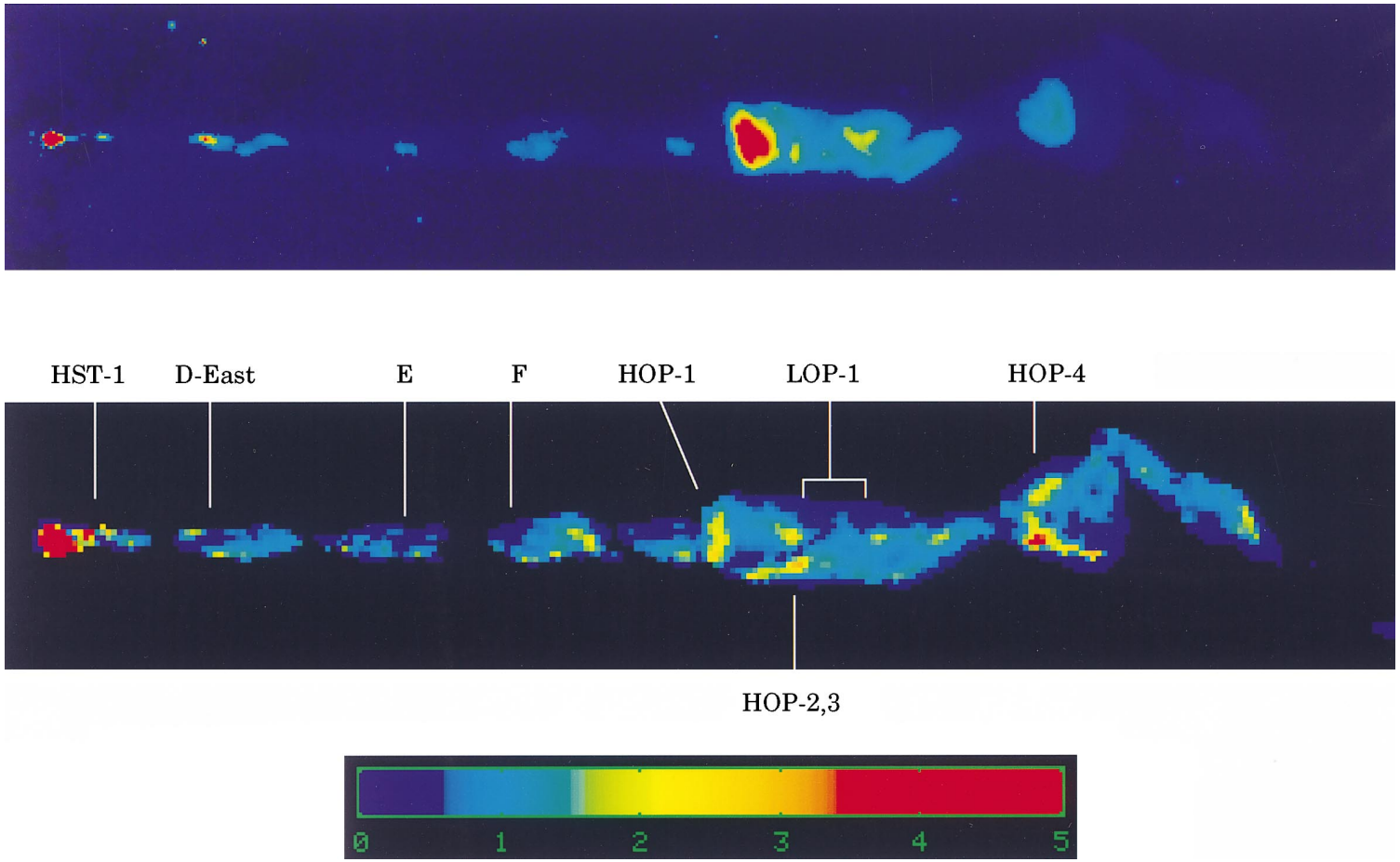

FIG. 2.—False-color representation of the ratio P_{opt}/P_{rad} (*bottom*). For reference, we also show the optical intensity map of Fig. 1*a* to the same scale (*top*). In the polarization ratio map, red regions indicate regions where the optical polarization is higher than the radio polarization, whereas deep blue regions are places where the radio polarization is higher. Considerable differences between optical and radio polarization values are observed in several areas, which we point out here. Of particular interest are the flux maxima of knots HST-1, D-East, E, and F, where the optical polarization decreases markedly (see § 5.1.1), and various features in knots A, B, and C (see § 5.2) which are denoted HOP or LOP depending on whether the optical polarization is higher or lower than the radio polarization.

somewhat lower spatial resolution, because of the instrumental configuration used. Another difference between this study and previous works (Thomson et al. 1995; Capetti et al. 1997) is that the radio map to which we compare our results was taken within 15 months of the optical observations. This helps to resolve some of the ambiguities noted in those papers.

In § 2, we will discuss the observational setup and data reduction procedures. Our results will be presented in §§ 3 and 4, and the physical implications discussed in § 5. In § 6, we conclude with remarks centering on the possible impact of future observations.

2. OBSERVATIONAL SETUP AND DATA REDUCTION

2.1. *HST Optical Polarimetry*

Optical polarimetry of the M87 jet was obtained on 1995 May 27 with the *HST* using WFPC2 and the F555W (broadband *V*) filter plus the POLQ polarization quad filter. The observational characteristics of the instrument are described by Biretta (1996). Essentially, WFPC2 is an imager with four chips arranged in a chevron. The PC1 chip has 0.″0455 pixels, and the three WF chips (WF2, WF3, and WF4) have 0.″09965 pixels.

In order to maximize the unvignetted field of view available for polarization observations, we used the WF chips, rather than the PC, for the polarization observations. For the same reason, we did not rotate the POLQ quad between observations. To obtain the Stokes parameters, it was then necessary to obtain images with all three WF chips, with each one representing an observation through a Polaroid nominally oriented at P.A. = 45°, 90°, 135° − V3, where V3 is the rotation of the *HST*'s *z*-axis with respect to the sky (for details, see Biretta & McMaster 1997). A total of 1800 s integration time, split in three to reject cosmic rays, were obtained in each WF chip. Within the same block of orbits, higher resolution PC images (2400 s integration) were obtained in the F555W and F814W bands. These data will be discussed in detail in a later paper (Perlman et al. 1999); however, the F555W PC image is presented in Figure 1*a* for reference, and we discuss it briefly in various parts of § 3 because its resolution is a factor of ∼2 better than possible with the WF chips only, and thus shows considerably more detail in compact regions.

The results of our optical and VLA polarimetry are shown in Figure 1. That figure includes four panels, which are, respectively, false-color representations of the optical total intensity and fractional polarization images, followed by the equivalent in radio. In all four panels, the same physical scale has been adopted, and the image has been rotated so that the jet is along the *x*-axis. We have marked on Figure 1 the location and traditional nomenclature for each of the major knots. In aligning the *HST* and VLA data sets, the nucleus was used as the fiducial point. The accuracy in the optical/radio registration should be ≈0.″02, i.e. $\sim\frac{1}{5}$ of a pixel, and is limited by the fact that the nucleus saturated all optical images taken. In Figure 2, we show a map of the polarization ratio $P_{\rm opt}/P_{\rm rad}$ for the jet. The angular scale used in this image is the same as used in Figure 1, so that the results can be directly compared. In Figures 3–6, we show optical and radio contour maps of various jet regions with magnetic field polarization vectors superposed. The Stokes *I* map used for those figures was produced with the WF images, rather than the PC, in order to avoid confusion resulting from differing resolutions.

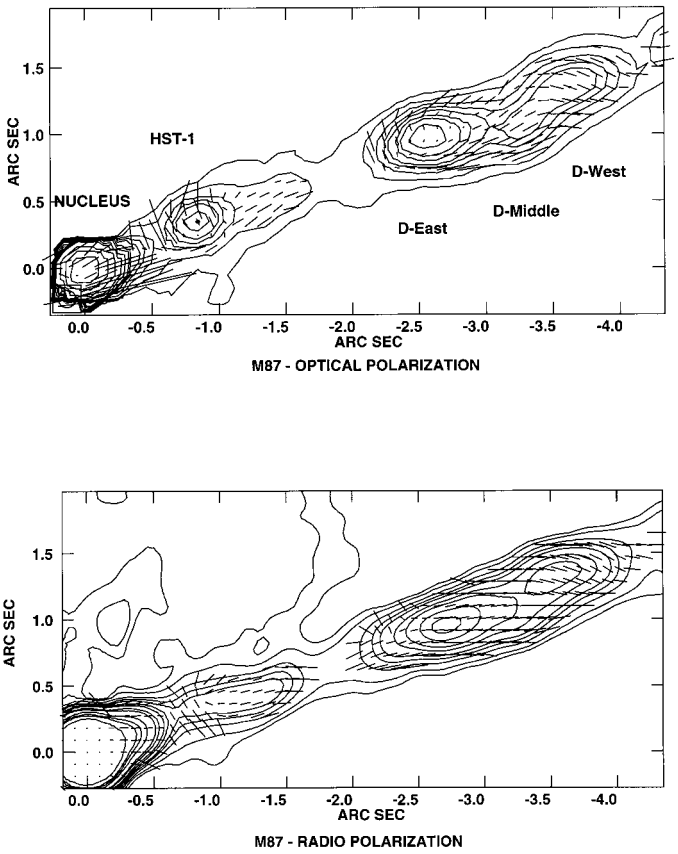

FIG. 3.—*Top*: Contour map of the optical structure of the innermost jet regions (including the nucleus, HST-1, and D), with magnetic field polarization vectors overlaid. A 1″ vector corresponds to 300% polarization. *Bottom*: Corresponding region in the radio. North is at the top, and east is at the left. The optical image is contoured at (1, 2, 4, 6, 8, 12, 16, 24, 32, 64, 128, 256) × 50 ADU pixel^{-1}, whereas the radio image is contoured at (1, 2, 4, 6, 8, 12, 16, 24, 32, 64, 128, 256) × 0.5 mJy beam^{-1}.

2.1.1. *Basic Data Reduction Techniques*

The *HST* data were recalibrated using the best available flat fields and dark-count images within STSDAS using standard techniques (Holtzman et al. 1995). Once this was done, the individual images were examined; it was found that as a result of pointing jitter, one of the three WF3 images was shifted by approximately 2 pixels, and so had to be shifted back. The data were then combined and cosmic rays rejected using the task CRREJECT. Once the data were flat-fielded and dark-count subtracted, the three images were geometrically rectified using the IRAF task WMOSAIC. After that, an 800 × 800 pixel section was cut out of each image, with the nucleus of M87 roughly at the center.

These subimages were then rotated so that north was along the *y*-axis, and then galaxy-subtracted. Galaxy subtraction was done using the tasks ELLIPSE, BMODEL, and IMCALC in STSDAS. To successfully model the galaxy, it was necessary to mask out the jet and SE hot spot, as well as all globular clusters and stars in the field. This is of necessity an iterative process, as the fainter globular clusters do not become apparent until galaxy subtraction is done. Failure to subtract a globular cluster would produce a circular "ringing" centered at the distance of the cluster.

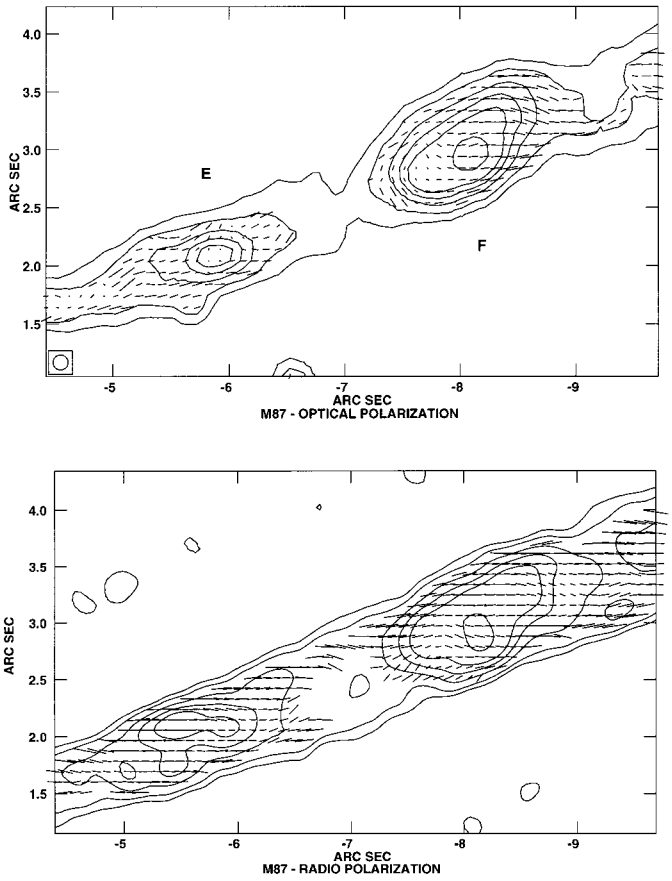

FIG. 4.—*Top*: Contour map of the optical structure of the knot E and F region of the jet, with magnetic field polarization vectors overlaid. A 1″ vector corresponds to 300% polarization. *Bottom*: Corresponding region in the radio. North is at the top, and east is at the left. The optical and radio images are contoured as in Fig. 3.

Once this was done, the resultant images were compared in detail. By measuring the FWHM of globular clusters that were essentially unresolved by the WFPC observations, it was determined that the WF2 observation had a PSF marginally narrower than the other two observations (2.05 pixels compared with 2.3 pixels), due to the redistribution of flux that occurs during the interpolations done by WMOSAIC and IMLINTRAN (both of which assumed the WF2 images as fiducial). To rectify this, the WF2 image was convolved with a circular Gaussian of 0.″13 FWHM. As a result of this procedure, we were able to determine that maximum resolution of these optical observations is 0.″23 FWHM.

2.1.2. *Polarization Calibration and Registration*

The most difficult part of the data reduction process was the astrometry required to combine the WF2, WF3, and WF4 images into Stokes *I*, *Q*, and *U*. High astrometric accuracy was required to eliminate residual errors. Several different methods were tried, including solutions with up to 40 globular clusters using several IRAF tasks and cross-correlation procedures. Even after the best fit from these procedures was produced, some additional tweaking was required (probably because of the undersampled PSF); this was done by hand by minimizing the "polarized" light from galactic regions in non–galaxy-subtracted images (checks using the polarization observed from globular clusters were also done).

To test not only the robustness of the registration over the entire image, we gradually "deregistered" both galaxy-subtracted and non–galaxy-subtracted images (along several directions), and then combined them according to the prescription given by the WFPC Polarization Calibration tool. The results of these tests confirmed that the WF images are correctly registered to within ± 0.15 pixel. Visual inspections of globular clusters near the edges of the 800×800 pixel image sections (i.e., images that were run through the polarization calibration tool) were done, to test the robustness of the registration in rotation. No shifts could be seen.

As a test of our polarimetric calibration we used aperture photometry to measure the fractional polarization of both the galaxy light and bright globular clusters in the image. All the results were consistent (within the uncertainties) with unpolarized emission, as one would expect.

Once properly registered, the three galaxy-subtracted WF images were combined using the WFPC2 Polarization Calibrator tool (described in Biretta & McMaster 1997) to produce Stokes *I*, *Q*, and *U* images. The tool takes into account not only the orientation of the *HST*, but also the instrumental polarization terms for all optical elements of the *HST*/WFPC2, including the pick-off mirror and the polarizer filter (which has a high cross-polarization transmission). Stokes *Q* and *U* images were then combined in a standard way to produce percent polarization [defined as $P = (Q^2 + U^2)^{1/2}/I$] and magnetic field position angle [defined as MFPA $= \frac{1}{2} \times \tan^{-1}(U/Q) + 90°$] images.

The resultant *P* image is shown in Figure 1*b*. This image has been clipped so that the fractional polarization is shown only for points with greater than 100 ADU (analog-to-digital unit) above galaxy.

2.1.3. *Uncertainties*

Because of the fact that the Stokes parameter images are each formed by linear combinations of the three galaxy-subtracted WF images, the Poisson uncertainty in *P* at any given point in the jet is approximately equal to the sum in quadrature of the Poisson errors in the counts on jet of any given feature (in each of the three WF images), plus the uncertainty due to subtracting the galaxy. Extensive testing (described below) determined that a third factor also contributes to the uncertainties in our data; this third factor is the uncertainty in registering the WF images. Here we discuss the relative impact of each of these uncertainties on our results.

The Poisson errors due to galaxy subtraction and photon noise vary widely from point to point along the jet, both as a result of the large range of surface brightness of jet features, as well as the relatively steep gradient and large signal from the galaxy. The signal from the galaxy (in Stokes *I*) varies from ~ 2600 ADU pixel^{-1} $\sim 1''$ from the nucleus, to ~ 300 ADU pixel^{-1} $\sim 25''$ from the nucleus. By comparison, the signal from the jet varies from only a few dozen ADU pixel^{-1} in some of the faint interknot regions of the inner jet, to nearly 6000 ADU pixel^{-1} in the brightest part of knot A. As a result, the dominant source of Poisson error is different in various regions of the jet. In the brightest regions of A, for example, the jet is far brighter than the galaxy, so that the Poisson error in *P* is dominated by the jet signal and is $\sim 1.5\%$ (note that the WFPC2 gain is 7 electrons ADU^{-1}). A similar situation pertains in lower surface brightness regions of A as well as B, where more

typical values for the signal are $\sim$1000–2000 ADU pixel^{-1} compared with $\sim$500–700 ADU pixel^{-1} from the galaxy. Poisson errors in these regions are more typically $\sim$3%. In the faintest regions of the outer jet, however (i.e., the interknot regions between knots B and C, or low surface brightness regions in the downstream part of knot C), the galaxy is much brighter than the jet and as a result the two contribute much more equally to the uncertainty. For example, in the interknot region between B and C, the galaxy signal is about 500 ADU pixel^{-1}, whereas only $\sim$50 ADU pixel^{-1} of jet emission is detected in each WF image (i.e., $I \approx 150$ ADU pixel^{-1}), so that the Poisson error due to galaxy subtraction is 5.6% and that due to the jet signal itself is 9.3%. Interior to knot A, the galaxy is brighter than the jet at every point. Nevertheless, the relative contribution of galaxy subtraction and jet to the Poisson errors still varies considerably. In the brightest parts of D (the brightest feature in the inner jet), for example, the signal from the jet is $\sim$500 ADU pixel^{-1} in each WF image, compared with about 2000 ADU pixel^{-1} (in Stokes I) from the galaxy, so that galaxy subtraction contributes a Poisson error of 1.1% and the jet contributes a Poisson error of 2.9%. The balance is somewhat different in lower surface brightness regions. For example, in the interknot regions between D and E, the surface brightness of the jet is 100–150 ADU pixel^{-1} (in I), whereas the galaxy at that point has a surface brightness of $\sim$1500 ADU pixel^{-1}. In these regions, the Poisson uncertainties from galaxy subtraction and the jet signal are about equal, and each is $\sim$10%. It is important to note that only in the lowest surface brightness regions do these two factors contribute about equally to the errors.

In most regions of the jet, the dominant contribution to our uncertainties comes from the registration of the three WF images, and not Poisson noise. The deregistration procedure described in § 2.1.2 also helped us establish the magnitude of this uncertainty, since one can closely examine the I, Q, U, P, and mosaic focal plane array (MFPA) images thus produced. The effect of a $\pm$0.15 pixel deregistration along the direction of the jet on the fractional polarization is $\delta P \lesssim 0.05$ (not 5%) in most jet regions, and $\delta P = 0.1$ in the region of knot A, where the intensity gradient is by far the largest of any region in the jet. The position angle is somewhat more stable: the effect of a $\pm$0.15 pixel deregistration along the direction of the jet on the position angle of polarization was $\lesssim 5^\circ$ throughout the jet. That this dominates the uncertainties in our result can be seen by comparing the size of this effect with the above figures for Poisson uncertainty, taking into account that the values we see for P range from 0.03 to $\sim$0.6 in the most heavily polarized regions. Only in the faintest regions of the inner jet do Poisson errors dominate.

The errors we quote herein on the optical polarization of individual resolution elements will include all of the abovementioned effects summed in quadrature. When examining larger regions, scatter will also be taken into account.

2.2. *VLA Radio Polarimetry*

Radio data were obtained at the VLA on 1994 February 4 using the A configuration. Only one intermediate frequency (IF; 14.435 GHz) was used, because of polarization calibration problems in the data in the other IF. The continuum correlator was used for this experiment, giving us a maximum bandwidth of 50 MHz. The total integration time was 10 hr. The observations also included a nearby phase calibrator, the flux and polarization calibrator 3C 286, and the closure error calibrator 3C 273. The observations were made with the phase center south of the jet, at R.A.(1950) = $12^h28^m17^s.000$, decl.(1950) = $12^\circ40'00''.00$.

The hybrid mapping process was started using CLEAN components from a previous observation in 1993 January at the same frequency (B95). This initial cross calibration serves to minimize differences in the data sets that might arise from calibration errors. Subsequent iterations of self-calibration should then remove any constraints incorrectly imposed by the cross calibration. Repeated iterations of MX and CALIB were done until a final map was obtained (see B95 and Zhou 1998 for further details)

At this point we used the bright point source in 3C 273 to calibrate the instrumental polarizations due to the antennas and feeds with PCAL in AIPS, and we used the 3C 286 data to calibrate the polarization position angles with CLCOR. After these solutions were applied, a final run of CLEAN was done. The final CLEAN image had 0".15 resolution and 0".045734 pixels (both identical to the image presented in OHC89). For direct comparison with the *HST* image, we have smoothed the radio image to 0".23 resolution and resampled to 0".09965 pixels. This improved the S/N, which was important in lower surface brightness regions. We show this image in Figures 1*c* and 1*d*.

3. OPTICAL POLARIZATION STRUCTURE

As can be seen in Figure 1, the jet is highly polarized over nearly all of its length. In the knot regions, $\langle P_{\rm opt} \rangle \sim 0.3$. Many of the knots have sections which are $\sim$40%–50% polarized, attesting to the highly ordered magnetic field structure which persists for well over 1 kpc from the nucleus. The most highly polarized regions of the jet are in knots HST-1, D, A, and B, which includes the brightest knots as well as those where superluminal motion has been found (B95; B99; Zhou 1998). Optical polarization parameters could not be computed for the nucleus, as the central 4 pixels were saturated. The optical MFPA direction in the inner jet (interior to knot A) is predominantly along the direction of the jet. However, close inspection reveals complex structure in each knot. The optical MFPA structure observed in the outer jet knots (A, B, C, and G) is very complex.

No polarized emissions are detected in the SE hot spot. However, this does not contradict previous results ($P = 0.34 \pm 0.05$; Sparks et al. 1992), as the surface brightness of the SE hot spot is only 30–35 ADU pixel^{-1} at maximum on our I image, compared with a signal of $\sim$350 ADU pixel^{-1} from the galaxy (i.e., 1 σ uncertainty in P of 0.33). We did attempt to search for compact, highly polarized emissions in this region by smoothing our Stokes I, Q, and U images with a Gaussian of 5 pixel FWHM. This improved the 1 σ uncertainty to $\delta P = 0.20$, but nevertheless no compact, highly polarized regions were detected.

Here we discuss our optical polarimetry results in the light of the optical morphology. We divide the discussion into subsections on the inner (interior to knot A) and outer jet, respectively, because as has been noted by many authors (e.g., SBM96 and references therein), the character of the jet changes drastically at knot A.

3.1. *The Inner Jet*

The morphology of the inner jet in both the optical and radio is dominated by five bright knot regions, usually

termed HST-1 (1″ from the nucleus), D (2.″5–4″ from the nucleus), E (6″ out), F (8″ out), and I (11″ out). Significant interknot emission is observed, although, as SBM96 have noted, the knot-to-interknot contrast is much higher in the optical than in the radio. We do detect polarized optical emissions in some of the interknot regions, but at relatively low significance ($\sim$2–3 σ). In the ensuing discussion, we will look at the characteristics we observe in each of the bright knots.

In the PC image shown in Figure 1*a*, knot HST-1 is characterized by a bright knot and fainter emission trailing downstream from the bright knot. Even higher resolution imaging and yearly monitoring by *HST* (B98; B99) resolves the fainter emission into several components, each of which appear to be moving superluminally with speeds up to 6*c*. Variability on 1 yr timescales is also observed in these knots (B98; B99). The resolution of our WF data (Fig. 3*a*) is not adequate to resolve individual, superluminally moving components. However, we clearly observe considerable structure in the first 2″ of the jet. These include low surface brightness emission extending $\sim$0.″5 from the nucleus, a bright knot at the position of the superluminal components ($\sim$1″ out), and fainter emission farther downstream. Inspection of Figure 3 also reveals some radio-optical morphological differences. In particular, in HST-1, the component at the upstream edge is brighter (relative to the rest of the knot) in the optical than in the radio, whereas downstream emission is brighter in the radio than in the optical. The MFPA appears parallel to the jet direction over the first 0.″5 downstream from the nucleus; however, the surface brightness of the jet is low in this region, and galaxy subtraction is almost certainly a dominant source of errors, as the galaxy gradient is extremely steep within 0.″5 of the nucleus. Immediately upstream of the HST-1 flux maximum, we observe $\langle P_{\rm opt}\rangle = 0.45 \pm 0.08$ and an MFPA orientation approximately perpendicular to the jet direction. Near the flux maximum, however, $P_{\rm opt}$ reaches a minimum of 0.14 ± 0.05 (averaged over a 2×2 pixel resolution element), i.e., we detect of polarization at the flux maximum at only the $\sim$2.8 σ level. Polarizations averaging $P_{\rm opt} = 0.41 \pm 0.08$ appear to be present at the north and south edges of the flux maximum region; however, we caution that our resolution is inadequate to resolve the width of this component, so the origin of these figures must await higher resolution data. Immediately downstream from the flux maximum, $P_{\rm opt}$ increases to 0.45 ± 0.08. The MFPA becomes parallel to the jet about 0.″3 downstream from the optical flux maximum in HST-1. In § 5.1.1 we discuss this constellation of properties (which also occurs in knots D, E, and F). The extremely high polarizations that appear to be present about 0.″5 from the nucleus are greatly affected by galaxy subtraction (the surface brightness of the galaxy at this point is $\sim$3500 ADU pixel^{-1}, whereas the jet is only $\sim$150 ADU pixel^{-1} in *I*).

We turn next to knot D, another highly active region, in which our *HST* monitoring (B98,B99) has revealed several components moving at apparent speeds up to 5*c*. Our data (Fig. 3*a*) reveal significant polarized structure in the knot D complex. At the upstream end of D-East, $\langle P_{\rm opt}\rangle = 0.30 \pm 0.06$, and the optical MFPA is perpendicular to the jet. Similarly to knot HST-1, we detect very little polarized optical emission ($P_{\rm opt} < 0.1$ is the 2 σ upper limit) at the position of the flux peak in D-East, and the polarization remains low in other interior regions of D-East. However, along the northern and southern edges of D-East, significant polarization is seen, with $P_{\rm opt}$ varying from 0.15 to about 0.60 (typical 1 σ error of 0.06), and the optical MFPA is primarily parallel to the jet axis. There is a peak at the southern edge of D-Middle where $P_{\rm opt}$ reaches 0.85; this value is likely affected by small number statistics and interpolation as this is a low surface brightness region of the jet. Just upstream from the flux maximum in D-West, the optical MFPA begins to rotate both at the edges and in the center of the jet; at the position of the flux maximum in D-West the optical MFPA is rotated by $\sim$45° and appears to remain roughly constant through the remainder of the knot.

Knot E, $\sim$6″ from the nucleus (Fig. 4*a*), is the faintest knot in the inner jet. The knot is characterized by lower surface brightness emission that begins about 1″ downstream from the western edge of knot D. The region of the flux maximum is unresolved in our WF observations (Fig. 4), but at the higher resolution of the PC image (Fig. 1) it is resolved into a double structure. The optical and radio emission (Fig. 3) are distributed somewhat differently, with the radio image showing a somewhat brighter eastern edge. Because of the low surface brightness of this feature, it is difficult to determine an average polarization figure for it. We can therefore only describe its polarimetric characteristics in more general terms. A few tenths of an arcsecond

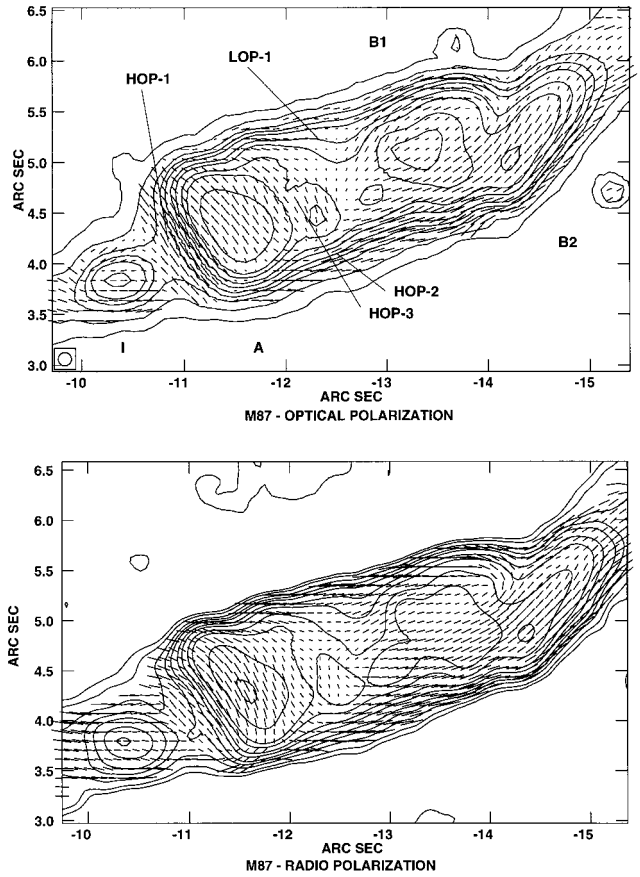

FIG. 5.—*Top*: Contour map of the optical structure of the knots I, A, and B, with magnetic field polarization vectors overlaid. A 1″ vector corresponds to 300% polarization. *Bottom*: Corresponding region in the radio. North is at the top, and east is at the left. The optical and radio images are contoured as in Fig. 3. The high and low optical polarization features in this region are labeled to avoid confusion.

upstream from the flux maximum, the polarization averages $\langle P_{opt} \rangle = 0.20 \pm 0.05$ with a generally east-west MFPA. Near the optical flux maximum, however, we do not detect appreciable polarization ($P_{opt} < 0.1$ at 2 σ). Downstream from the flux maximum, we observe $\langle P_{opt} \rangle = 0.15 \pm 0.05$ and an MFPA within $\sim 20°$ of the jet direction. However, the data are quite noisy in this region.

Knot F is significantly but not completely resolved at the 0.″2 (Fig. 4*a*) resolution of the WF images. At higher resolutions (Fig. 1*a*), it shows a diffuse double structure, with the brighter region farther from the nucleus. The polarized fraction at the upstream edge of the knot F complex is modest ($P_{opt} = 0.15 \pm 0.05$) and barely at the 3 σ level, but we consider its detection significant because of the consistency of the MFPA observed across this region, where it is perpendicular to the jet. Near the position of the first flux peak, no polarization is detected (as in D and HST-1); however, at the position of flux maximum (the second peak in Fig. 1*a*), P_{opt} has reached 0.20 ± 0.05 (the scatter on individual points is lower), and increases steadily in the downstream part of the knot complex, reaching a maximum at the northwest edge of knot F, where an average polarization of $P_{opt} = 0.36 \pm 0.06$, and peaks in individual pixels of $P_{opt} \approx 0.45$, are seen. Similarly to knot D, the optical MFPA becomes perpendicular to the jet direction at the upstream edge of the knot. Along the northern and southern edges, the optical MFPA is initially parallel to the jet but rotates slightly about $\sim 0.″5$ downstream of the head of the knot to become very nearly east-west. The mostly east-west ***B*** field persists until the trailing edge of the knot region, where the MFPA rotates by about 45°.

Knot I (Fig. 5), $\sim 11″$ from the nucleus, is modestly polarized ($\langle P_{opt} \rangle \approx 0.15 \pm 0.05$). Slightly higher values of P_{opt} are observed along its northern and southern edges (0.20 ± 0.05 and 0.26 ± 0.05, respectively; an unresolved peak of 0.41 ± 0.07 is seen near the southwestern edge). About 0.″3 upstream of the optical peak, we see a rotation by 20° in the optical MFPA, to a nearly east-west orientation; except at the northern edge of the knot, where it is well aligned with the jet direction.

3.2. *The Outer Jet*

Knot A (Fig. 5*a*) has a highly complex structure, dominated by a bright, broad shock. Over most of this region, and especially along the jet axis, the ***B*** field is parallel to the shock front, which is inclined 18° to the jet normal. Typically $P_{opt} = 0.35 \pm 0.03$ (uncertainty determined by scatter only, because of the size of the region; the single-pixel maximum is $P_{opt} = 0.47 \pm 0.10$) in the brightest regions. In fact, the region with ***B*** parallel to the shock front starts about 0.″7 upstream of the flux maximum, and interestingly, the most highly polarized portion of knot A is 0.″5 upstream of the optical flux maximum, corresponding to the preshock "bar" region (using the terminology of B98). Here we observe an average polarization $P_{opt} = 0.53 \pm 0.07$, peaking at a single-pixel maximum of 0.59. Although we must stress that our 0.″2 resolution is not adequate to resolve the bar from the strong gradient at the upstream edge of A, we find this feature highly interesting. We will comment further on it in § 5.2.1. Here we note only that it is important for this feature to be confirmed by higher resolution FOC observations. We have scrutinized the pre-COSTAR FOC observations of Capetti et al. (1997) for information on this region; those authors do not specifically comment on this region in their text but an inspection of their maps reveals it to be highly polarized. We observe a somewhat lower polarization region ($P_{opt} \sim 0.30$) separating the "bar" region from the flux maximum. The degree of polarization in the jet interior decreases gradually downstream of the bright shock, and the optical MFPA remains roughly aligned with the shock in this region. The edges of the jet in knot A have a more complex behavior than the interior. Throughout the edges, P_{opt} is more modest than in the brightest regions, averaging ~ 0.15. The MFPA rotates significantly as one moves from the jet center toward the edges, even at positions equidistant from the nucleus compared to the flux maximum. This rotation reaches almost 90° (***B*** parallel to the jet axis) in jet-edge regions about 0.″5 downstream from the flux maximum; a similar MFPA orientation is not observed in the jet interior until one moves downstream by another 0.″5.

Knot B, 14″ from the nucleus (Fig. 5*a*), is also complex. It has two bright regions: B1, which is closer to the nucleus and near the jet axis, and B2, which is downstream from B1 and at the southern edge. Knot B2 is somewhat more polarized than B1, with P_{opt} averaging 0.34 ± 0.05. The most heavily polarized regions of knot B are at the edges, particularly the southern edge, where $\langle P_{opt} \rangle = 0.45 \pm 0.05$ and the single-pixel maximum is 0.54. The interior of the jet and particularly B1 is only modestly polarized, with P_{opt} averaging 0.22 ± 0.07. But even within B1, the southern part is more heavily polarized, reaching a maximum of 0.41 ± 0.05 near the southwestern edge of B1. Within B1, the MFPA is

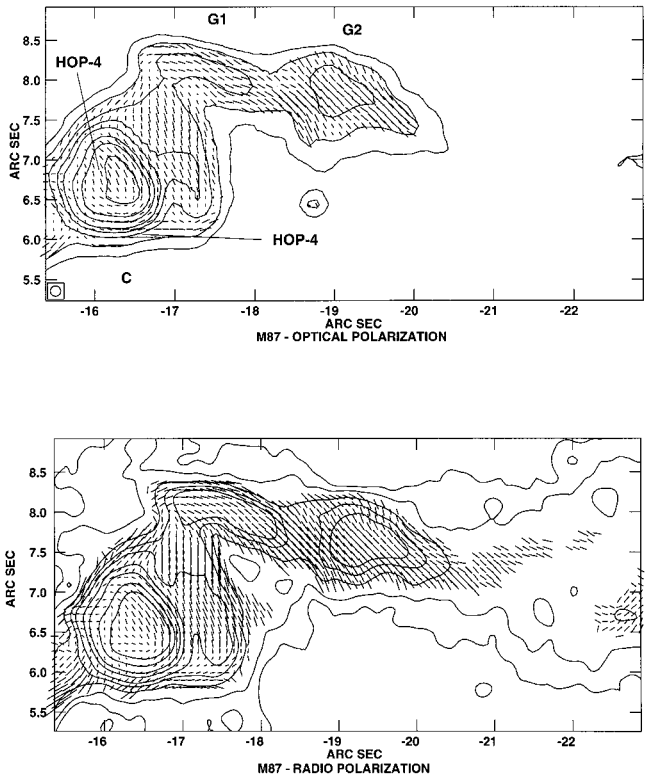

FIG. 6.—*Top*: Contour map of the optical structure of knots C and G, with magnetic field polarization vectors overlaid. A 1″ vector corresponds to 300% polarization. *Bottom*: Corresponding region in the radio. North is at the top, and east is at the left. The optical and radio images are contoured as in Fig. 3. The high and low optical polarization features in this region are labeled to avoid confusion.

oriented parallel to the jet direction. However, $\sim 1''$ downstream of the optical flux peak of B1, the MFPA becomes perpendicular to the jet. The MFPA is parallel to the jet in B2 and also in other lower surface brightness regions of B. We will comment further on these properties in § 5.2.2.

Knot C (Fig. 6) is located 17″ from the nucleus. It is characterized by a bright, rhomboidally shaped region $\sim 1''$ long, which is wider at the downstream end. The jet itself flares somewhat in this region, its width increasing by nearly a factor of 2 in about 2″. A second, fainter shock (which can be seen at higher resolutions, e.g., Fig. 1) appears at the downstream edge of the flaring region. We observe fairly complex polarization structure in C. $P_{\rm opt}$ reaches a minimum all along the eastern and northern edges of the rhomboidal main shock; these regions can be seen quite easily on Figure 6 and have $P_{\rm opt} < 0.10$ at 2 σ (see § 5.2.2 for further discussion). The most heavily polarized, bright part of knot C is just downstream from the flux maximum, where $P_{\rm opt}$ reaches 0.30 ± 0.04 (uncertainty determined by scatter). Comparably high polarizations (averaging 0.26 ± 0.05 and peaking at 0.36) are observed at the downstream edge of the knot, where the MFPA remains perpendicular in the jet interior. The MFPA assumes a nearly perpendicular orientation near the upstream edge of the main shock region, but it is parallel to the jet along the northern and southern edges of the entire knot C region.

Knot G, 20″ from the nucleus, has very low surface brightness and is characterized by two diffuse knots, often called G1 and G2 (Fig. 6). We detect fairly high polarization (at relatively low significance) throughout both G1 and G2, with $\langle P_{\rm opt} \rangle = 0.30 \pm 0.10$. The MFPA appears to be oriented within 30° of the jet direction throughout knot G.

4. RADIO POLARIZATION STRUCTURE

We now turn to the radio data. Since OHC89 have already given detailed descriptions of the structure (both total and polarized flux) in various jet regions, here we discuss only regions where significant changes are observed. As the main emphasis of this paper is on the polarized structure, we will only detail structural changes in general terms. For a more detailed analysis of proper motion and variability, the reader is referred to Zhou (1998).

The radio morphology of the inner 2″ of the jet has changed markedly since 1985 (Fig. 3*b*). The most noticeable change is the appearance of a bright region that begins 0.″8 from the nucleus and extends for nearly 1″. This feature, which corresponds roughly to the location of the HST-1 region, can also be seen on the 1993 January 11 map shown in B95. This change in structure is most likely the result of motions in the jet, consistent with our findings (B98; B99) of components with speeds up to 6*c*, which vary on 1 yr timescales, in HST-1. By comparison, the 1985 map showed a relatively bright region that began 1.″1 from the nucleus and extended for about 0.″8 (OHC89).

The radio MFPA in HST-1 is perpendicular to the jet axis at the position of the first peak, but within 0.″3 resumes a generally parallel orientation. Interestingly, no significant deviations from a parallel orientation were seen in the first 2″ of the jet in the 1985 map (OHC89). Throughout the HST-1 complex, $P_{\rm rad}$ remains modest, ranging from 0.13 to 0.33 and averaging 0.21. This behavior is significantly different from that observed in the optical and is dealt with in § 5.1.1.

A change is also noticeable in the knot D complex (Fig. 3*b*), where the separation between knots D-East and D-West (measured peak-to-peak) has changed from 0.″76 (OHC89) to 1.″04. This is very close to the value of 1.″12 measured by Capetti et al. (1997) on pre-COSTAR *HST* images; we therefore assert that the radio-optical differences in the structure those authors noticed were largely due to temporal evolution. We believe this evolution is likely to include both motion and variability, rather than just motion (which, if alone responsible, would imply a speed of 7.9*c*). The peak of emission in D-East appears to be about 0.″2 closer to the nucleus in our 1994 image than in the 1985 image. In addition, knots D-Middle and D-West are known to move superluminally with speeds $\sim 2.1c$–$2.5c$ (B95) in the radio. The combination of these two easily explains the change in D-East to D-West distance we see (see Zhou 1998 for a deeper analysis).

At the upstream end of D-East, the radio MFPA is approximately parallel to the jet direction. A $\sim 20°$ rotation (to nearly east-west) can be seen beginning near the flux peak of D-East and continuing through D-Middle. Significant rotation is seen in D-West, similar to what is seen in the optical (§ 3.1). As in HST-1, the degree of polarization varies little ($\langle P_{\rm rad} \rangle = 0.32$, maximum $P_{\rm rad} = 0.45$) throughout the knot D complex and does not reach a minimum near the flux maximum of D-East as observed in the optical (see § 5.1.1).

The degree of polarization in F (Fig. 4*b*) in the radio varies considerably more than in knots HST-1 and D, ranging from 0.11 to 0.50, and averaging 0.26. There has been very little change in the overall polarization structure of knot F in the 9 yr between the OHC89 map and ours; however, because our S/N is somewhat higher, some additional detail is revealed. In both, the radio MFPA remains roughly east-west from the flux peak downstream (similar to the optical). No evidence for rotation of the radio MFPA can be seen at the upstream edge of the knot. At the western edge, our higher S/N allows to see some evidence for a slight rotation in the MFPA, similar to what is seen in the optical, but considerably smaller in magnitude. We also see considerable polarized emission in the interknot region between knots F and I, where the radio MFPA is oriented in the east-west direction.

5. IMPLICATIONS

Polarimetry provides clues to the direction of the magnetic field within the jet, as well as the character of the plasma flow. Hence it is one of the most important diagnostics for deciphering jet structures. Comparisons between polarimetry results in different bands give us important further insights into the internal structure of the jet. In particular, since previous *HST* observations have already shown that optical emission in the M87 jet is more concentrated along the jet axis, a comparison of optical and radio polarimetry results gives us the opportunity to learn about the magnetic field structure as a function of distance from the jet axis.

5.1. *Physical Processes in the Inner Jet*

The majority of the differences between our optical and radio polarimetry results occur in the inner jet. Several properties are common to more than one jet region. We will discuss such regions together.

5.1.1. *Knots HST-1, D, E, and F*

Significant differences are present in the optical and radio

polarization structures of knots HST-1, D, E, and F (Figs. 3 and 4). First, the degree of polarization varies less in the radio than in the optical. The average optical polarization just upstream of the flux peak in HST-1 is $\langle P_{\rm opt} \rangle = 0.45 \pm 0.08$, while at the maximum, $P_{\rm opt}$ drops to just 0.14 ± 0.05. Similarly, in D, E, and F, $P_{\rm opt}$ values of 0.15–0.30 are observed just upstream of the flux peaks, compared with less than 0.10 at the flux peaks. By comparison, $P_{\rm rad}$ is much more stable, averaging 0.24 ± 0.07 upstream of the flux peak in HST-1 compared with 0.15 at the flux peak. A similarly small change is observed in F, where $P_{\rm rad}$ drops from 0.30 ± 0.09 to 0.20 ± 0.07 at the position of the flux peak, although note that there is a local minimum of 0.11 0.″2 farther south. The drops in $P_{\rm rad}$ observed at the flux peaks of D and E are statistically insignificant. At the upstream ends of knots HST-1, D, and F, the optical MFPA rotates to a direction nearly perpendicular to the jet, whereas the radio MFPA remains primarily along the jet axis in D and F. At the downstream edges of these components, the MFPA are generally more similar in the radio and optical.

M87 is not the only object where high polarization and perpendicular MFPA is observed near the upstream edge of bright knots, and the polarization decreases near the flux maximum. Similar properties are observed in radio observations of the inner jet of Cen A (Clarke, Burns, & Norman 1992). Unfortunately, no three-dimensional view of those structures is yet available due to the large optical obscuration present in Cen A.

The differences in the optical and radio polarization characteristics we observe are clear evidence that the optical and radio emission seen from the jet originate in somewhat different physical regions. In Figure 7, we illustrate a model for the physical situation in these knots. The critical features of this model are (1) that the $\boldsymbol{B}$-field direction varies as a function of distance from the jet axis and (2) that the optical and radio synchrotron-emitting electron populations are not completely colocated. The optical emission is dominated by the bright, "shocklike" regions (likely in or near the jet center), where $\boldsymbol{B}$ is perpendicular to the jet axis as a result of compression of the magnetic field. By comparison, the radio emission is dominated by less energetic electrons near the jet surface, where $\boldsymbol{B}$ is parallel to the jet axis possibly as a result of shearing of field lines against the external medium. In this model, the $P_{\rm opt}$ in bright regions will either be low or have MFPA perpendicular to the jet axis, depending on the relative intensities of the $\boldsymbol{B}$ parallel surface emission and the $\boldsymbol{B}$ perpendicular emission near the jet center.

Taken by themselves, our radio data do not contradict the model proposed by OHC89 (which was proposed for the 1985 radio data). The OHC89 model postulates a surface layer with uniform emissivity ~ 0.1 times the jet width, a negligible interior emissivity, and a bright filament wrapped helically around the jet to create the asymmetry. However, the OHC89 model cannot explain the differences we observe between the optical and radio polarization structure in knots HST-1, D, E, and F (above), nor can it explain the subtle but significant morphological differences (e.g., higher knot-to-interknot region contrast; SBM96) in the inner jet. Indeed, it is very difficult if not impossible to explain the differences in polarization structure under any model where the radio- and optical-emitting electron populations are colocated.

It is important to note that our model does not contradict the idea that Kelvin-Helmholtz instabilities play an important role in generating many of the features in the M87 jet. Whereas the energy input from the Kelvin-Helmholtz mechanism peaks at the jet surface (Hardee 1983), the pressure perturbation for axisymmetric helical ($n = 1$) Kelvin-Helmholtz modes reaches maximum well inside the jet sheath. The compression of the magnetic field would be expected to vary closely with the pressure. Therefore, we would expect to observe synchrotron-emitting electrons with the highest energies in interior regions of the jet where the pressure perturbations reach maximum.

Several groups have explored largely similar models for active jet regions (Cawthorne & Wardle 1988; Cawthorne & Cobb 1990; Fraix-Burnet & Pelletier 1991; Gómez et al. 1994a, 1994b, 1995, 1997; Hardee & Norman 1988; Hardee & Clarke 1995; Hardee, Clarke, & Rosen 1997; Hughes, Aller, & Aller 1985, 1989, 1991; Mioduszewski, Hughes, & Duncan 1997; van Putten 1996). Although they differ in details, all postulate a shock propagating along the jet, usually with a propagation speed somewhat slower than the overall flow speed. In shocked regions, the magnetic field is compressed, resulting in a more organized field oriented approximately normal to the jet. As was pointed out particularly by Gómez et al. (1994b), it is by no means necessary for the shock to encompass the entire jet flow. The picture shown in Figure 7 fits quite well with a scenario whereby the shocks we observe in the inner jet only take up a fraction of the axial breadth of the jet. This is also consistent with the observation that the emission in these knot regions is highly concentrated close to the jet axis (SBM96).

The wealth of structure we see offers further clues as to the nature of these shocks. Quite clearly knots D and F cannot be explained as simple shocks, given their size, complex structures, and velocity fields (B98; B99). This is particularly true for knot D, given its complexity (Fig. 1) and the fact that superluminal components have been found over its entire length (B95; B98; B99).

One interesting possibility is that the shock features may not necessarily be perpendicular to the overall jet direction. Two features suggest this: the decrease in the degree of optical polarization at the flux peak, and the rise in the degree of polarization (accompanied by some rotation of the $\boldsymbol{B}$ field) at the trailing edge of knots HST-1, D, and F. The models of Cawthorne & Cobb (1990) and Fraix-Burnet & Pelletier (1991) allowed the orientation of planar shock regions to vary (in the other papers mentioned above, shock regions were assumed to be perpendicular to the jet direction) and attempted to predict observable features. Cawthorne & Cobb (1990) show that under such a model, the degree and direction of polarization observed in various regions would be highly geometry-dependent. A perpendicular MFPA would be observed at both the upstream and downstream ends. Along the side edges of such a shocked region, the observed MFPA would be parallel to the jet direction. This model also predicts the observed decrease in polarization at the flux maxima of these components, because the position of the flux maximum also represents the position where the plane of compression of the magnetic field most nearly approaches our line of sight. At this position, significant cancellation would be observed in the projected magnetic field (see Gómez et al. 1998 and Cawthorne & Cobb 1990 for discussions). We note also that Doppler boosting could produce brightening by a factor of 10 or more given the speeds observed in knots HST-1 and D

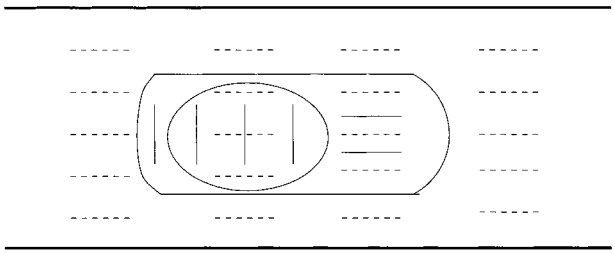

FIG. 7.—Magnetic field in M87 jet and knots. Here we illustrate a model which we believe explains many of the differences we see both in structure and polarization in the inner jet. *Dashed lines*: Surface of jet, brightest in radio. *Solid lines*: Surface of jet, brightest in optical. A key aspect of this model is that optical- and radio-emitting electrons are not completely colocated; the optical-emitting electrons are located closer to the jet axis, whereas most of the radio-emitting electrons are located nearer the jet surface. Our polarimetric results suggest significant differences in the magnetic field structures in these regions. See § 5.1.1 for further discussion.

(B98, B99). It is possible that the tracks taken by knots within the jet may be curved, perhaps helical, and that the plane of compression of the magnetic field in each of these shocks is somewhat inclined with respect to the jet direction (but is most likely perpendicular to the helical track followed by the knots). Shocked regions of the jet could also be the sites of in situ particle acceleration, wherein a considerable hardening of the optical spectrum would be observed (e.g., Begelman & Kirk 1990). We have in fact observed this in our multicolor *HST* photometry (Perlman et al. 1999).

5.1.2. *Knot I*

In knot I (Fig. 5), we see much more similar magnetic field orientations in the radio and optical; both bands show largely east-west MFPA and a small decrease in the degree of polarization at the flux peak. The situation at the trailing edge of knot I is more difficult to assess because both the radio and optical maps show evidence that the polarized emissions from knot A begin only 0.″5 downstream of the flux peak in knot I. These properties do, however, suggest that the shock which produces knot I is a smaller perturbation than those which produce the other inner jet knots.

5.1.3. *Interknot Regions*

The high degree of polarization we observe in interknot regions of the inner jet (typically 20%–40%; Fig. 1) indicates that the magnetic field in relatively undisturbed regions remains highly ordered. The interknot regions do not show a significant tendency for lower polarizations nearer the jet center (although note that in our maps the jet is unresolved across its width through the entirety of the knot D region). This property is similar to what is observed in the first 27″ (12 kpc) of the NGC 6251 jet (Perley, Bridle, & Willis 1984), as well as in the inner few kiloparsecs of most other low-luminosity radio galaxies' jets (e.g., Cen A, Clarke et al. 1992; 3C 31, Laing 1998). Perley et al. (1984) cite this property, as well as a small expansion rate, as evidence of a high Mach number (>10) in the inner regions of the NGC 6251 jet; we suggest that a similarly high Mach number flow may be present in the inner M87 jet.

5.2. *The Outer Jet*

As many previous authors have noted (SBM96 and references therein), the appearance of the M87 jet changes drastically at knot A. From this point outward, the jet emission is not so highly concentrated in a few fairly compact knots. We observe very high optical and radio polarizations (close to 50%) in the outer regions of knot B (Fig. 5), as did OHC89. OHC89 point out that this property is evidence of lower synchrotron emissivity in the jet core in this region. An increase in jet polarization at the outer edges of the jet might also be evidence of torsional shear, which could not as easily be observed in the center of the jet because of cancellation of different field directions seen in projection. Bicknell & Begelman (1996) have modeled knot A as a torsional shock that is eventually responsible for the disruption of the jet flow observed beyond C. Our data are consistent with such a picture. The torsional shock model is fully consistent with the structure in the MFPA (which follows the jet contours at the outer edges), as well as with the suggestions made by OHC89 regarding the state of matter in the core regions of the outer jet. Such features may be common in AGN jets, since similar features exist in the polarized emissions of at least one other jet (Cen A; Clarke et al. 1992).

Our data show that the outer and inner jet differ in another way: the magnetic field structures seen in optical and radio observations of the outer jet are much more similar than in the inner jet. In a global sense, this is an indication that the optical and radio-emitting electron populations in the outer jet are more closely colocated than in the inner jet. Close examination of Figures 5 and 6 does, however, reveal a few differences, most of which are also pointed out as high or low optical polarization regions in Figure 2. We will detail the implications of these differences below, dealing with knot A separately, as some controversial claims have been made regarding its structure.

5.2.1. *Knot A*

High polarization is seen along the edges of knot A (Fig. 5), as well as near the flux peak. Both the optical and radio maps show large changes in the MFPA ($\sim 70°$), between knot I and the bright, broad shock that houses the optical and radio flux peak of knot A. The degree of polarization begins to increase about 0.″2 closer to the nucleus in the optical than in the radio; this can be seen in our vector map as well as the depolarization image (region HOP-1; Figs. 2 and 5). The rotation of the $\boldsymbol{B}$-field vectors also starts $\sim 0.''2$ earlier in the optical. Our maps also show some differences between the optical and radio morphology of A, which were previously noted by SBM96. In particular, the upstream end of the shock region has a concave appearance in the radio which does not evidence itself in the optical. While the flux peaks are coincident, the abrupt brightening at the leading edge of knot A occurs slightly earlier in the optical than in the radio. Also, as noted by SBM96, the jet through this region appears somewhat narrower in the optical than in the radio, at least at the intermediate and upper contour levels.

These slight differences between the optical and radio polarimetry could be explained if the disturbance which illuminates the jet at knot A begins in the jet interior and spreads to the entire breadth of the jet within about 0.″3 (20 pc). Under this scenario, evidence of the disturbance would be seen slightly earlier in the optical, where higher energy electrons are concentrated (as indicated by the inner jet appearing narrower in the optical; see § 5.1.1 and SBM96). The strongly compressed magnetic field in this region could

produce in situ particle acceleration, which would yield a much harder spectrum at the upstream edge of knot A. This might also explain why the X-ray emission from knot A appears to be located approximately 0.″5 short of the optical and radio maximum (Neumann et al. 1997). *Chandra X-Ray Observatory*/HRC observations are required to test this hypothesis.

Owen & Biretta (1998) have produced a very high resolution (0.″035) radio map of the M87 jet at 7 mm, with the VLA in the A array. Those data show that the sharp feature at the leading edge of knot A is narrower than their minimum resolution of ~ 3 pc. One possible interpretation of the Owen & Biretta (1998) result might be that this feature is a filament wrapped around the jet surface, rather than a shock. However, three observations reported here and in other papers argue against this interpretation. First, the extremely steep gradient in flux at the leading edge of knot A, and the strongly elevated flux downstream of its flux maximum (relative to the inner jet), is much more characteristic of a shock than a filamentary feature. A second argument that strongly suggests the presence of a shock within knot A is the marked change in the appearance of the jet (as several authors have noted); beyond knot A, the jet takes on a more "filled" appearance. But perhaps the most persuasive argument of all comes from the polarization vector maps (Fig. 5), which show MFPA parallel to the leading edge of the flux maximum region for more than 1″ downstream. Such a configuration is inconsistent with identifying the sharp feature with a $\sim 0.''03$ wide filament, but well in accordance with the presence of a bright shock that affects the downstream region.

Thomson et al. (1995) claim that there is a region of high depolarization at the northwestern edge of knot A. Close examination of the polarization ratio map (Fig. 2) does reveal two small "depolarization" features near the western edge of the knot, which we have labeled HOP-2 and HOP-3; these features have also been noted on Figure 5. These features lie within the boundaries of the depolarization feature claimed by Thomson et al. (1995), but near its upstream edge. They are nowhere near as large nor as deep as the region claimed by Thomson et al. (1995), as close comparison of our Figure 2 and their Figure 5 shows (we observe maximum depolarization of ~ 2–3 compared with values of $\gtrsim 5$ reported by Thomson et al.).

Our results do confirm that some "depolarization" (low radio polarization) is present at the downstream edge of knot A. However, since our results indicate much smaller differences than did Thomson et al., we are forced to conclude that their claim of a large mass of Faraday-active material at the northwestern edge of knot A is probably in error and may have been produced by misalignment of the radio and UV images. Further evidence for poor radio/UV image alignment can be seen in their UV-radio spectral index map (their Fig. 4), which appears to show a "steeper" spectrum at the upstream ends of knots F, I, and A. This conflicts with the UV-radio spectral index map made from higher S/N (but still pre-COSTAR) data, which included the nucleus, shown in SBM96. Such an error may have occurred because Thomson et al. aligned the radio and UV images by cross-correlating the optical and radio jet structures. As has already been noted, the optical and radio structures are subtly different; the differences between the two might well produce an apparent offset of $\sim 0.''1$ toward the northwest in the *HST* data. We also note that comparison of 5 and 8 GHz VLA images (Zhou 1998) show no excess Faraday rotation or depolarization in this region.

Both "depolarization" features are much more consistent with variations in the energy spectra of emitting electrons as a function of distance from the jet center, as illustrated for various regions of the inner jet in § 5.1. In particular, the low radio polarization in HOP-2 and HOP-3 may simply reflect that the radio emission is returning to its ***B*** parallel configuration sooner after knot A, than the optical emission. This transition region would, of course, have low polarization, since there is blending of parallel and perpendicular emission. That the transition occurs earlier in the radio may be attributable to shearing at the jet surface, together with the fact that the jet appears broader in the radio, as noted before. The extra component of ***B*** parallel emission from the jet surface seen in the radio would tend to make the perpendicular-parallel transition following knot A, occur earlier.

5.2.2. *Knots B, C, and G*

Throughout the remainder of the outer jet, the optical and radio polarimetry results track each other extremely well. In both the radio and the optical data, the highest polarization regions of knot B are along the edge, and the MFPA is identical. The story is similar throughout most of knots C and G. However, when one looks in more detail, some small differences appear.

At the northwestern edge of the region between knots A and B, the degree of polarization remains high in the radio while in the optical, it becomes nearly undetectably low (this region can also be seen in the depolarization map; we have labeled it LOP-1). Immediately downstream from this region, we see the optical MFPA rotate 90° (while the radio MFPA remains approximately east-west), and after about 0.″4 it tracks the radio MFPA extremely well. As can be seen by inspection of the vector plots, this occurs about 0.″8 upstream of the flux maximum in B1. Capetti et al. (1997) pointed out that the magnetic field in this region of the jet is highly tangled, and there is significant structure on scales smaller than 0.″2, as seen on their 0.″06 resolution map (their Fig. 5). When observed at only 0.″2 resolution, significant cancellation would take place, explaining the low optical polarization we observe.

At the northwestern edge of knot B1, the optical polarization decreases somewhat more rapidly than the radio (but not dramatically so). That this is the result of cancellation of magnetic field vectors can be seen by inspecting Capetti et al.'s 0.″06 resolution map, which shows an 0.″2–0.″3 scale magnetic "loop" in this region. The opposite thing happens near the flux maxima of knots B1 and B2, where the degree of polarization is slightly higher in the optical than the radio. In both of these last features, the optical and radio MFPAs remain consistent with one another.

There is a fairly large region of low radio polarization at the extreme eastern edge of knot C, which we have labeled HOP-4 (Figs. 2 and 6). This can be seen particularly along the southeastern edge of the knot, where the optical polarization is somewhat higher and the magnetic field direction follows the flux contours quite well. Inspection of Figures 1, 2, and 6 reveals that this occurs just after the broad minimum reached by both $P_{\rm opt}$ and $P_{\rm rad}$ at the upstream edge of knot C. It can be seen by close inspection of Figure 1 that $P_{\rm opt}$ increases slightly quicker than $P_{\rm rad}$, suggesting that this shock too may begin in the jet interior. This would

require that (similarly to the situation analyzed above for many inner jet regions) higher energy, optical synchrotron-emitting electrons must be concentrated along the shocked surfaces which are evident as the bright regions of knot C (particularly at the eastern edge). Any particle acceleration would affect higher energy regions of the jet first, and hence evidence itself first in the optical.

6. CONCLUSIONS

The data and analysis we present has given us the first hints regarding the three-dimensional magnetic structure of extragalactic jets. From previous modeling efforts, one would have naively expected the magnetic fields observed in the optical and radio to be largely similar, indicating that the high and low energy electron populations are largely cospatial. This was expected particularly because (1) the energy input from magnetosonic instabilities (including Kelvin-Helmholtz) peaks in the jet sheath (e.g., Hardee 1983), and (2) radio observations had suggested that the emissivity in the center of the M87 jet was much smaller than in its sheath (OHC89). The present observations reveal a quite different picture: there are clear differences between the optical and radio polarization structures of knots HST-1, D, E, and F, particularly at their upstream "shocked" edges and at their flux maxima. At the upstream ends of these regions, we tend to observe perpendicular magnetic fields in the optical only (in the radio, the MFPA remains parallel to the jet), whereas near their flux maxima the degree of optical polarization declines precipitously. As previously shown (SBM96), the radio and optical synchrotron-emitting electron populations occupy somewhat different regions of the jet, with the optical-emitting populations not only more concentrated in the knots, but also closer to the jet axis. Hence a natural explanation for the radio/optical polarization differences we observe is that the jet contains significant internal magnetic structure. Namely, that parallel fields predominate near the jet surface, while perpendicular fields are present in the knots near the jet axis, where the field lines are strongly compressed.

Our observations reveal much more similarity in the optical and radio polarimetry beyond knot A. This is a strong indication that the nature of the jet changes drastically at this point, as many other authors have previously commented. This leads us to believe that the processes which create the main emission features in the inner and outer jet must be somewhat different in nature, with considerable contributions from shocks in the inner jet, whereas the outer jet more dominated by torsional and/or Kelvin-Helmholtz instability, as suggested by OHC89 and Bicknell & Begelman (1996).

The high polarizations that we observe are evidence that even in the interknot regions, the magnetic field remains highly ordered. The overall characteristics of the interknot regions are somewhat different in the outer jet than they are in the inner jet. In the inner jet, we do not observe a general tendency for the jet center in these regions to be less polarized than the edges, whereas beyond knot A, this characteristic is observed both in the optical and radio. This is consistent with a high Mach number flow in inner regions of the jet, but a somewhat lower Mach number beyond knot A.

Considerable scope remains for future observations of the M87 jet, based on the *HST* results pointed out in this and other papers (SBM96; B98; B99). This study represents the strongest evidence yet that the structure of extragalactic jets is stratified in electron energies. Since the optical-emitting regions seem to be concentrated much closer to the jet axis than radio-emitting regions (this work), and are more compact (SBM96), one would expect an increasing compactness at the highest energies. The subarcsecond resolution of the *Chandra*/HRC will offer us the opportunity to test this prediction by measuring the width of the jet beyond knot A as well as pinpoint the location of knot A's X-ray maximum, which some authors (Neumann et al. 1997) indicate may be somewhat closer to the nucleus, perhaps in the region where we see very high optical polarization in these observations. Similar tests will also be possible in knot B, but not for the inner jet, which is far too narrow to be resolvable with *Chandra*.

Further scope also remains for *HST* observations. Not only is significant secular evolution occurring in several regions of the jet (HST-1 and D in particular; see B98, B99), but also our resolution ($\sim 0\farcs2$) is insufficient to separate out superluminally moving components in these regions. Higher resolution observations would separate individual superluminal components, and more fully resolve other details of the magnetic field structure where we have noted these data have insufficient resolution. It would be particularly interesting to monitor the evolution of these components as they move out. The spectral energy distribution should soften as each component cools and harden as particles are accelerated and as new superluminal components are born. Moreover, the magnetic field should also respond to such changes, giving detailed information about the degree of fluid and magnetic field compression with time (see Gómez et al. 1994a, 1994b). Ongoing and future *HST* observations should test these possibilities.

REFERENCES

Baade, W. 1956, ApJ, 123, 550
Begelman, M. C., & Kirk, J. G. 1990, ApJ, 353, 66
Bicknell, G. V., & Begelman, M. C. 1996, ApJ, 467, 597
Biretta, J. 1993, in Astrophysical Jets, ed. D. Burgarella, M. Livio, & C. O'Dea (Cambridge: Cambridge Univ. Press), 125
———. 1996, The WFPC2 Instrument Handbook (1996 June ed.; Baltimore: STScI)
Biretta, J., & Junor, W. 1995, Proc. Natl. Acad. Sci., 1995 December
Biretta, J. A., & McMaster, M. 1997, WFPC2 Instrument Science Report 97-11 (Baltimore: STScI)
Biretta, J., Perlman, E. S., Sparks, W. B., & Macchetto, F. 1998, in M87: Picture of a Radio Source, ed. H.-J. Röser (Heidelberg: Springer), in press (B98)
Biretta, J., Sparks, W. B., & Macchetto, F. 1999, ApJ, in press (B99)
Biretta, J., Zhou, F., & Owen, F. 1995, ApJ, 447, 582 (B95)
Böhringer, H., Nulsen, P. E. J., Braun, R., & Fabian, A. C. 1995, MNRAS, 274, L67
Boksenberg, A., et al. 1992, A&A, 261, 393
Capetti, A., Macchetto, F. D., Sparks, W. B., & Biretta, J. A. 1997, A&A, 317, 637
Cawthorne, T. V., & Cobb, W. K. 1990, ApJ, 350, 536
Cawthorne, T. V., & Wardle, J. F. C. 1988, ApJ, 332, 696
Clarke, D. A., Burns, J. O., & Norman, M. L. 1992, ApJ, 395, 444
Fanaroff, B. L., & Riley, J. M. 1974, MNRAS, 167, 31P
Fraix-Burnet, D., Le Borgne, J.-F., & Nieto, J.-L. 1989, A&A, 224, 17
Fraix-Burnet, D., & Pelletier, G. 1991, ApJ, 386, 87
Gómez, J. L., Alberdi, A., & Marcaide, J. M. 1994a, A&A, 284, 51
Gómez, J. L., Alberdi, A., Marcaide, J. M., Marscher, A. P., & Travis, J. P. 1994b, A&A, 292, 33
Gómez, J. L., Marscher, A. P., Alberdi, A., Marti, J. M., & Ibanez, J. M. 1998, ApJ, 499, 221
Gómez, J. L., Marti, J. M. A., Marscher, A. P., Ibanez, J. M. A., & Alberdi, A. 1997, ApJ, 482, L33
Gómez, J. L., Marti, J. M. A., Marscher, A. P., Ibanez, J. M. A., & Marcaide, J. M. 1995, ApJ, 449, L19
Hardee, P. E. 1983, ApJ, 269, 94

Hardee, P. E., & Clarke, D. A. 1995, ApJ, 449, 119
Hardee, P. E., Clarke, D. A., & Rosen, A. 1997, ApJ, 485, 533
Hardee, P. E., & Norman, M. L. 1988, ApJ, 334, 70
Holtzman, J. A., et al. 1995, PASP, 107, 156
Hughes, P. A., Aller, H. D., & Aller, M. 1985, ApJ, 298, 301
———. 1989, ApJ, 341, 54
———. F. 1991, ApJ, 374, 57
Laing, R. L. 1998, in 39th Herstmonceux Conference, Relativistic Jets in Astrophysics, ed. R. Laing (Cambridge: Cambridge Univ. Press), in press
Mioduszewski, A. J., Hughes, P. A., & Duncan, G. C. 1997, ApJ, 476, 649
Neumann, M., Meisenheimer, K., Röser, H.-J., & Fink, H. H. 1997, A&A, 318, 383
Owen, F. N., & Biretta, J. 1998, in M87: Picture of a Radio Source, ed. H.-J. Röser (Heidelberg: Springer), in press
Owen, F. N., Hardee, P. E., & Cornwell, T. J. 1989, ApJ, 340, 698 (OHC89)
Perley, R. A., Bridle, A. H., & Willis, A. G. 1984, ApJS, 54, 291
Perlman, E. S., Biretta, J. A., Sparks, W. B., & Macchetto, F. 1999, in preparation
Reid, M. J., Biretta, J. A., Junor, W., Muxlow, T. W. B., & Spencer, R. E. 1989, ApJ, 336, 112
Schlötelburg, M., Meisenheimer, K., & Röser, H.-J. 1988, A&A, 202, L23
Sparks, W. B., Biretta, J., & Macchetto, F. 1996, ApJ, 473, 254 (SBM96)
Sparks, W. B., Fraix-Burnet, D., Macchetto, F., & Owen, F. N. 1992, Nature, 355, 804
Stiavelli, M., Biretta, J., Möller, P.,& Zeilinger, W. W. 1992, Nature, 355, 802
Thomson, R. C., Robinson, D. R. T., Tanvir, N. R., MacKay, C. D., & Boksenberg, A. 1995, MNRAS, 275, 921
Tonry, J. L. 1991, ApJ, 373, L1
van Putten, M. H. P. M. 1996, ApJ, 467, L57
Warren-Smith, R. F., King, D. J., & Scarrott, S. M. 1984, MNRAS, 210, 415
Zhou, F. 1998, Ph.D. thesis, New Mexico Inst. Mining Tech.